PAPER • OPEN ACCESS

Transition of piezoresistive gauge factor tuned by lateral size in MoS$_2$ and WS$_2$ networks

To cite this article: D Olaya-Cortes *et al* 2025 *2D Mater.* **12** 025002

View the article online for updates and enhancements.

You may also like

- Mechanical properties of transition metal dichalcogenides: towards high-performance polymer nanocomposites
  Dimitrios G Papageorgiou, Ming Dong, Han Zhang et al.

- A review on transfer methods of two-dimensional materials
  I Cheliotis and I Zergioti

- When 2D materials meet metals
  Luka Pirker, Jan Honolka, Matj Velický et al.

2D Materials

CrossMark

Transition of piezoresistive gauge factor tuned by lateral size in MoS$_2$ and WS$_2$ networks

D Olaya-Cortes [ID], C Navarrete, T Rubio [ID], P Giraldo-Gallo [ID] and Y Hernandez[*] [ID]

Physics Department, Nanomaterials Laboratory, Universidad de los Andes, Bogota 111711, Colombia
* Author to whom any correspondence should be addressed.

E-mail: yr.hernandez@uniandes.edu.co

Abstract

Transition metal dichalcogenides (TMDs) are a family of layered two-dimensional materials which find great interest in fields such as medicine, energy conversion, water treatment, and electronics. Nevertheless, the interesting properties that arise as the number of layers is reduced, do not necessarily persist when the nanosheets are printed on substrates to form networks. Therefore, research on the networks and the influence of the nanosheets' dimensions is valuable for scaling up prospects. It is known that strain alters the band structure of TMDs and also tune transitions between different crystal structures. The figure of merit that measures how much the resistivity changes when strain is applied is the gauge factor (*GF*). In networks, this is modeled as a sum of the nanosheet intrinsic *GF* and the change of the junction resistance between nanosheets due to strain. In this work we obtain the *GF* of devices printed on polyvinylidene fluoride membrane filters through their transport characteristics when applying uniaxial strain, both at a tensile and a compressive setup, by using a three-beam bending machine. We report a transition from a positive *GF* to a negative one, when applying uniaxial strain to WS$_2$ networks as the lateral size increases, and a transition from negative *GF* to a positive one, when compression is applied to MoS$_2$ networks as lateral size increases.

1. Introduction

Strain is a multifaceted parameter crucial for controlling and tuning the properties and structures of two-dimensional materials, such as graphene and transition metal dichalcogenides (TMDs). As a result, it is a prominent topic in condensed matter physics. Strain enables band structure modifications, including transitions from direct to indirect bandgaps for uni-axial strains less than 2% [1, 2] or a semiconductor-to-metal transitions when tensile bi-axial strain between 10% and 15% is applied [3]. It also alters phonon vibrations, observable in the Raman signal [4], and facilitates exciton funneling when applied inhomogeneously, since optical features depend on local band structure variations, directing the excitons towards regions of maximum strain [5]. Furthermore, optoelectronic parameters like responsivity, electroluminescence, emission wavelength, and differences between bright and dark excitons can be fine-tuned by applied strain [6–9].

Strain detection is an appealing field with significant applications in human motion detection, the diagnosis of oral diseases [10], and energy conversion [11–13]. This strain sensing is typically attributed to either the piezoelectric effect, where strain-induced polarization changes generate an electric field, or to the piezoresistive effect, which involves change in resistance due to alterations in the band structure under strain. The sensitivity of strain sensing is often measured using the gauge factor (GF), defined as the ratio of the relative change in resistivity to the applied strain $((\Delta R/R)/\epsilon)$. A higher gauge factor indicates greater sensitivity in detecting strain through resistance changes, thereby improving detection accuracy [11].

TMDs have emerged as promising materials for piezoresistive applications [14–16], due to their excellent flexibility and their ability to withstand strains before breaking [11, 13]. In a seminal study by Tsai *et al*, the piezoresistive response of field-effect (FET) tri-layer molybdenun disulfide (MoS$_2$) transistors

was measured, showing a gauge factor of -40 when applying a gate bias of 20 V [17]. The key observation centered around the shift in the representative current-*versus*-voltage curve of the transistor when subjected to mechanical strain. The resulting piezoresistive effect arises from variations in the band gap of the MoS_2, which were evident through shifts in the optical reflection spectrum.

Furthermore, Manzeli *et al* explored the impact of mechanical strain on the electronic properties of mono-, bi-, and tri-layer MoS_2 nanosheets (NS). Strain was applied using an atomic microscope tip, favoring simultaneous measurements of current and tip deflection. Remarkably, the gauge factor exhibited distinct values: -148 for mono-layer, -224 for bi-layer, and -43.5 for tri-layer MoS_2. The intriguing observation lies in the superior gauge factor of the bi-layer configuration. This enhanced sensitivity arises from the stronger interaction between the Mo d_{z^2} orbitals in the two Mo planes within the bi-layer structure [18].

Reproducibility in manufacturing remains a significative challenge in strain sensing [13], as gauge factors and initial resistance can vary across sensors produced from the same batch. Yokaribas and coworkers demonstrated that increasing the number of layers in chemically vapor-deposited graphene enhances reproducibility by reducing defect density [19]. Additionally, they developed devices using graphene nanoplatelets (GNPs) and found that when the network density exceeded the percolation threshold, variations in the GF decreased. In such networks, strain alters tunneling distances, thus modifying the conductive pathways.

The efficiency of strain transfer is another critical challenge. Slippage and strain relaxation can interfere with the desired strain application, posing potential risks when using flexible or elastomer substrates [11, 14]. Wagner *et al* and Zhang *et al* studied selenide-based TMD sensors, which were transferred or deposited on polymer substrates [20, 21]. These sensors are coupled to a bending test machine, similar to methods used in [14, 22], to tune the electronic properties of TMDs. Wagner reported a gauge factor of -85 for platinum diselenide ($PtSe_2$) [20], while Zhang found a gauge factor of -315 for palladium diselenide ($PdSe_2$). In the latter study, the authors successfully deposited the material on the polymer substrate, thereby reducing the transfer step, which could introduce defects detrimental to the sensor, and enhancing stability for over 10000 cycles [21].

Another challenge that has been tackled by researchers is the understanding of the sensitivity at high strains [23, 24]. Biccai *et al* conducted a comprehensive study on TMDs composites, specifically combining it with polyethylene oxide (PEO). Their investigation revealed compelling piezoresistive behavior,

which transitioned from reduced resistivity at low applied strain to increased resistivity beyond the yield strain, higher than 10%. In the elastic regime of the composites, the piezoresistive behavior was primarily governed by the intrinsic piezoresistive nature of the TMD [23]. Above the yield strain, the piezoresistivity increased, which is attributed to an increased particle separation, reducing the probability of tunneling between particles.

Riyajuddin and colleagues designed and developed a strain sensor based on a heterostructure of graphene and graphitic carbon nitride [24]. This device addresses the challenge of the strain operation range, as most strain sensors exhibit linear behavior only under small strains. Although the gauge factor is relatively low at 1.89, the sensor can endure strains exceeding 25% showing a linear trend. The periodic nanopores in the graphitic carbon nitride structure induce polarization changes upon strain application, while the polydimethylsiloxane (PDMS), as a highly stretchable polymer, enhances the sensor's ability to withstand large deformations [24].

As has been discussed, the gauge factor of the TMDs is negative, this means that the resistivity decreases as tensile strain is applied. However, the behavior of TMDs under strain is multifaceted, and positive gauge factors have also been observed. Zhang *et al* focused on tungsten disulfice (WS_2) drawn on paper subjected to a controlled uniaxial strain. Surprisingly, these devices exhibited positive gauge factor. The underlying mechanism lies in the behavior of the material, for when subjected to stretching the distance between particles increases, thus increasing the resistivity of the device [22].

The stability of the device is another key challenge in strain sensing. By encapsulating molybdenum diselenide ($MoSe_2$) printed on paper with PDMS, Selamneni and coauthors added both surface protection and flexibility [25]. This device was tested as both a pressure and strain sensor, achieving a sensitivity of 0.3 kPa^{-1} and a gauge factor of 6.84. The device maintained its resistivity for 500 cycles, with the authors attributing the piezoresistive effect to the tunneling between $MoSe_2$ nanosheets forming a network.

The final challenge in strain sensing lies in advancing theoretical and experimental work on TMD-based sensors to develop models and experiments that explore strain effects beyond the typical low-strain regime and conventional strain transfer methods. In this regard, the research by Shi *et al* and Varghese *et al* is groundbreaking [10, 26]. Shi and colleagues created a heterostructure of tungsten disulfide nanosheets with molybdenum disulfide quantum dots soaked to a thermoplastic polyurethane/multi-wall carbon nanotubes foam. This multifunctional device senses gas and pressure changes and was engineered for

diagnosing oral diseases [10]. The sensor exhibited two different gauge factors depending on the strain percentage: 1.4 for strains in the range of 10%−60%, and 3.2 for strains in the range of 80%−160%.

Varghese and coworkers demonstrated strain transfer by coupling a piezoelectric thin film to a 3-layered MoS_2 FET, facilitating easy measurement of the gauge factor [26]. In their study, applying compressive strain resulted in a negative gauge factor, while tensile strain produced a positive value, reaching −1500 and 1000, respectively. These studies provide the latest evidence of shifts in resistivity sensitivity due to strain [10, 26] attributed to the anisotropic structure of the 3-layered MoS_2.

Our work adds to the needed experimental work that shows tuning of the gauge factor with a controlled external parameter, such as, the dimensions of the TMD nanosheets [27]. We first state the experimental details to produce dispersions of TMDs by the method of liquid phase exfoliation aided with lithium-ion intercalation and to print devices from those dispersions. Furthermore, the methodology of measuring the piezoresistivity in TMDs networks is briefly described and the results of the characterization of piezoresistivity are shown. TMDs networks show interesting features such as a transition from positive to negative gauge factor (*GF*) tuned by the size of the nanosheets, which could help in the understanding and design of sensors used in applications where different type of gauge factors are needed. Furthermore, the conductivity of these networks is shown, and its description allows to understand a few details on the piezoresistive effect that these networks display.

2. Experimental details

Tungsten disulfide (WS₂, Merck, 2 μm, 99%), molybdenum disulfide (MoS₂, Merck, powder), lithium hydroxide (LiOH, Merck, reagent grade, $\geqslant$ 98%) and ethylene glycol were obtained from commercial sources. The intercalation process begins with the mixing of TMD powders (specifically WS₂ and MoS₂) with lithium hydroxide (LiOH). The stoichiometric ratios were optimized to obtain high-concentration dispersions: 0.77 mg of LiOH per mg of WS₂ and 1.2 mg of LiOH per mg of MoS₂. Furthermore, 15 ml of ethylene glycol were added to the mixture. The entire reaction takes place within an autoclave. For our experiments, the initial mass of WS₂ was 130 mg and the initial mass of MoS₂ was 100 mg.

The TMD powders underwent a h heat treatment at 200 °C, facilitating the diffusion of lithium ions into the TMDs layers. Subsequently, the mixture was subjected to a thorough cleaning procedure by vacuum filtration through a polyvinylidene fluoride (PVDF) filter with a pore size of 0.1 μm (sourced

from Durapore, with a diameter of 25 mm). This step effectively removed any residual ethylene glycol and unused intercalation products, ensuring the purity of the TMDs.

The lithium-intercalated TMDs were next combined with N-Methyl-2-pyrrolidone (NMP) and subjected to sonic bath exfoliation for one hour. To further enhance the concentration, during the next hour of exfoliation for WS₂ (and the next two hours for MoS₂) the solvent was mixed with deionized water (at a ratio NMP:H₂O of 70:30). This adjustment aimed to bring the surface tension of the solvent closer to the interlayer van der Waals forces of the TMDs, thereby increasing the overall exfoliation efficiency [28].

The last step of the production involved a 24 h decantation process. After this period, the supernatant, containing the desired exfoliated TMD dispersion was carefully collected. Simultaneously, the sediment, which contained impurities and lithium ions, was removed. This systematic approach ensures the production of high-quality TMD dispersions [27, 29].

In this investigation of the impact of nanosheet size on piezoresistivity [27], dispersions from both TMDs were synthesized using the liquid cascade centrifugation method [30–32]. The centrifugation process was carried out at three distinct speeds: 500 rpm, 1 krpm and 1.5 krpm. The procedure commenced by obtaining a sample of the dispersion produced by intercalation and exfoliation process. This initial sample was subjected to centrifugation at 500 rpm for 2 h. As a result, the supernatant, containing nanoflakes of smaller dimensions than those within the sediment, was carefully collected. Subsequently, this supernatant underwent a second centrifugation step, this time at 1 krpm for 2 h. Meanwhile, the sediment was redispersed in an NMP aqueous solution. The same iterative process was applied to the supernatant and sediment from the 1 krpm centrifugation step, but this time at a higher speed of 1.5 krpm. By systematically varying the centrifugation speeds, different dispersions were achieved, each characterized by a distribution of decreasing average lateral-size NS (Refer to figure S1 of supporting information showing SEM images and their distribution).

The second step in this investigation involves device preparation [27, 29]. During this step, a precisely measured quantity of each dispersion is vacuum-filtered through a PVDF membrane filter. The PVDF membrane has a diameter of 47 mm and a pore size of 0.22 μm, which is sufficient to retain nanosheets larger than its pore size on the filter. The outcome of this filtration is the formation of a uniform layer atop the PVDF filter. Subsequently, the filter is carefully dried using a heating plate set at 45 °C for one hour. To establish electrical contact with the TMD layer, two copper wires are securely attached

to the plane using copper tape. These contacts are positioned at a known distance from each other. The choice of copper is deliberate: its significantly higher conductivity compared to TMDs layers ensures the establishment of an ohmic contact [12].

Regarding the characterization of the TMDs, Raman spectroscopy measurements, which result from the inelastic scattering of photons by molecules of the material [33], were performed on the devices. Furthermore, the number of layers of both TMDs was extracted by interpolating and comparing with previous reports [34, 35]. The Raman spectra of the devices were obtained using a Horiba XploRA confocal Raman microscope with an incident light of wavelength of 532 nm and power of 0.7 mW, obtaining 10 accumulations, each in an acquisition time of 10 s. The range of the detected signal was $200 - 800$ cm^{-1}.

To measure the piezoresistive effect, the most common technique is to apply strain through tensile testing and measuring the resistivity by a source-meter unit (SMU). This is advantageous because the stress can also be measured while measuring the resistivity as a function of strain [23]. Another technique to measure this effect is to apply the strain with a controlled deflection of the substrate, as proposed by Castellanos-Gomez [22]. This can be achieved by using a three-beam bending setup which relates the deflection, D, the length between pivotal points, L, and the thickness of the substrate, t, to the applied strain ε, by 1:

$$\varepsilon = \frac{6Dt}{L^2}. \tag{1}$$

Using this setup, a tensile uniaxial strain was applied to the upper part of the device, which rested on the middle beam during the bending process [27], as shown in figure S2(a). The opposite end of the copper wires was connected to a Keithley 2450 SMU to measure the current–voltage (IV) curve of the device. The electrical contacts were placed far from the middle beam of the three beam set-up, to make sure that the strain was only applied to a region where only the TMD was strained [12]. The measurements were taken from an unstrained configuration to a bending configuration of 3 mm, resulting in a tensile strain of 1.6%. The bending process was carried out incrementally in steps of 0.3 mm. When this process was finalized, the device was turned upside down, thus the upper part would be in a compressive strain, and the same steps were done to study the effect with both types of strains.

3. Results and discussion

To investigate the vibrational modes of the TMDs on the devices, Raman spectroscopy was performed on them [27]. As shown in figure 1(a), the spectrum for
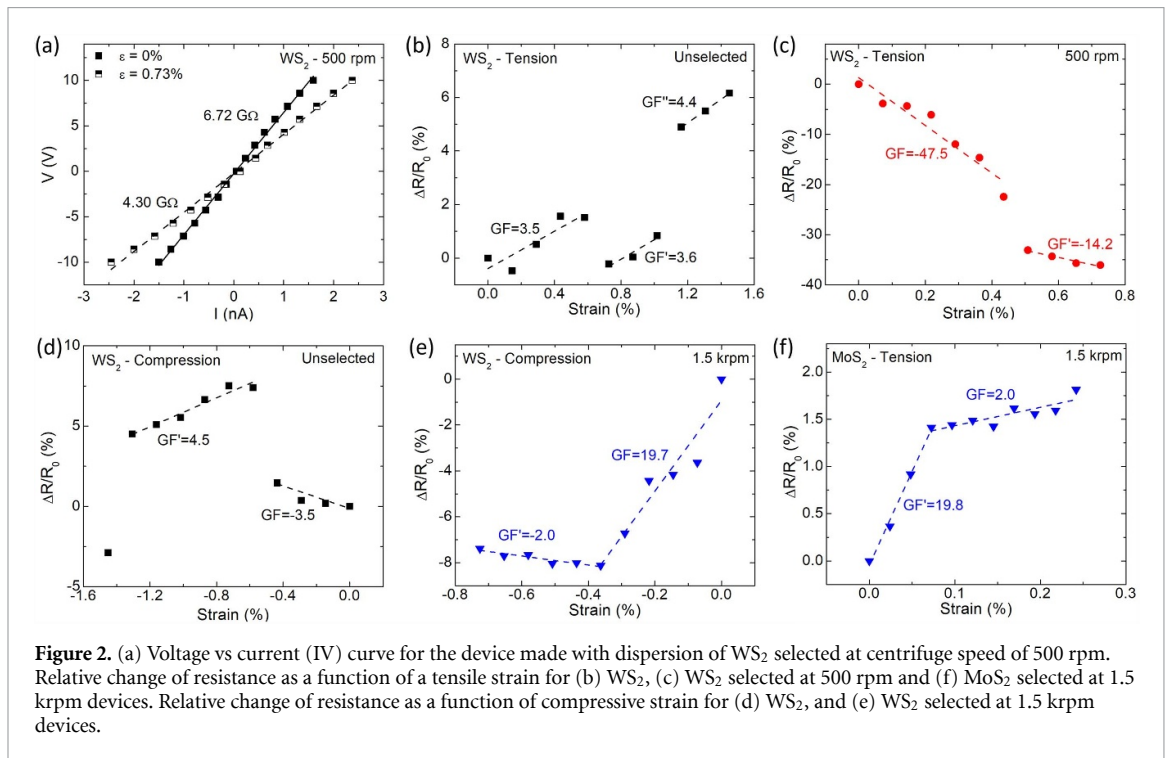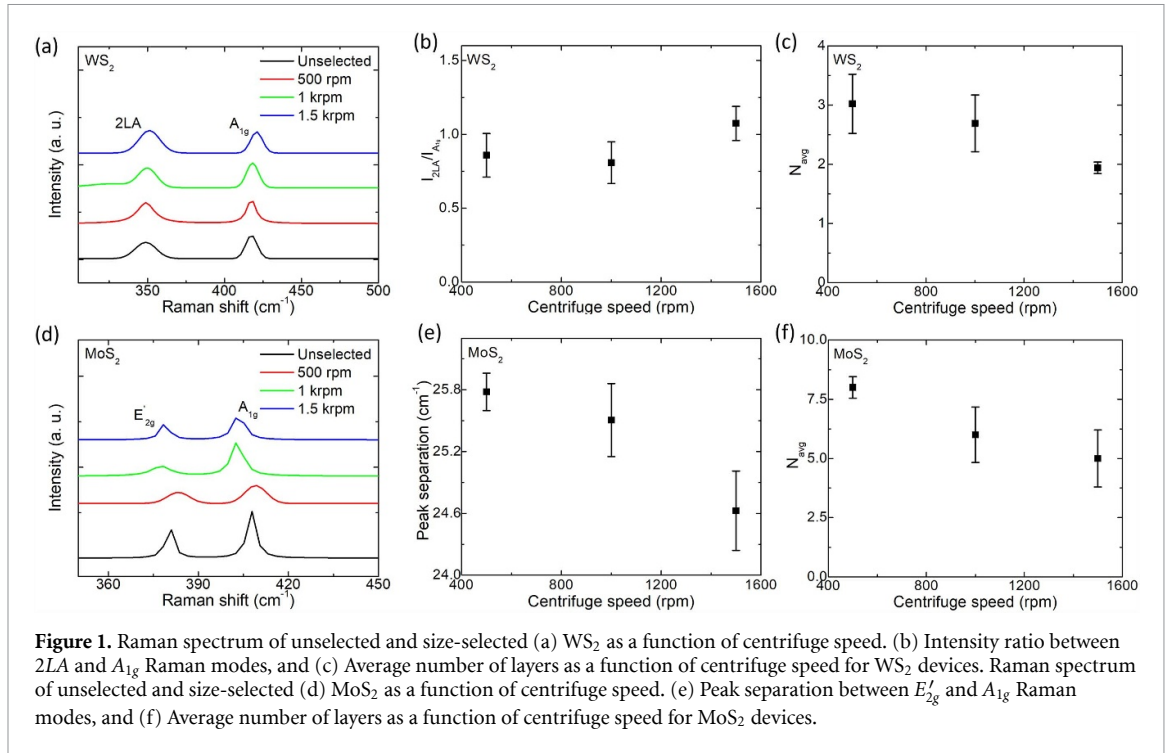
WS$_2$ shows the second order longitudinal acoustic mode 2*LA* and the first order A_{1g}. The former corresponds to compressions and expansions in the plane of tungsten disulfide that move along the direction of propagation, while the latter correspond to out-of-plane vibrations [34]. Whereas for MoS$_2$ (Refer to figure 1(d)), the characteristic features that appear in the spectrum are the in-plane vibrations E'_{2g} and the out-of-plane vibrations A_{1g} [35].

The Raman spectrum is used as a metrology tool to determine the number of layers, as these vibrations are dependent on this feature [34, 35]. Therefore, the ratio of intensities between the vibrational modes is calculated in WS$_2$ and MoS$_2$. The frequency and intensity of these features are extracted from Lorentzian fits of the Raman spectra. As the centrifuge speed decreases, the intensity ratio of both peaks decreases (refer to figure 1(b)). This was observed on mechanically exfoliated nanosheets by Berkdemir and coworkers as the number of layers increases [34]. This was attributed to a reduction of the intensity of the longitudinal mode and an increase of the intensity of the out-of-plane mode. From this data, a calculation of the thickness of the layers is extracted as shown in figure 1(c). Large, medium, and small nanosheets have average thicknesses of 3 layers, between 2 and 3 layers, and 2 layers, respectively.

Regarding MoS$_2$, the metric used to extract the average number of layers was the separation between the characteristic vibrational modes. As shown in figure 1(e), as centrifuge speed decreases, the difference between peaks increases. This was observed previously in mechanically exfoliated MoS$_2$ when the number of layers increases. Furthermore, a difference between peaks close to 24.6 cm^{-1} as observed for our devices separated at a speed of 1.5 krpm, is corresponding to 5 layers. Comparing the intensity ratio of A_{1g} and E'_{2g} Raman modes and the separation between peaks, with the work of Li and coworkers [35], the calculation of number of layers is done in figure 1(f).

Medium lateral size nanosheets have an average of 6 layers, while large size nanosheets have an average of 8 layers. As can be seen, for MoS$_2$ nanosheets, the number of layers is away from the mono-layer regime, thus the exciton features become less effective [31], and the shift of the exciton peak is much reduced as compared with WS$_2$ devices, which we have observed for our dispersions in our work on photoconductive properties of networks of TMDs [29].

Figure 2(a) illustrates the transport properties of the device when no strain is applied and at a tensile strain of 0.73% on the device made with WS$_2$ dispersion selected at 500 rpm. The figure reveals that the resistance is lowered when the strain is applied. Typically, the change in transport for piezoelectric devices arises from either the relative change in position of the crystals [22, 36], thus changing the junction resistance, or from the strain applied to the

Figure 1. Raman spectrum of unselected and size-selected (a) WS$_2$ as a function of centrifuge speed. (b) Intensity ratio between 2LA and A_{1g} Raman modes, and (c) Average number of layers as a function of centrifuge speed for WS$_2$ devices. Raman spectrum of unselected and size-selected (d) MoS$_2$ as a function of centrifuge speed. (e) Peak separation between E'_{2g} and A_{1g} Raman modes, and (f) Average number of layers as a function of centrifuge speed for MoS$_2$ devices.

Figure 2. (a) Voltage vs current (IV) curve for the device made with dispersion of WS$_2$ selected at centrifuge speed of 500 rpm. Relative change of resistance as a function of a tensile strain for (b) WS$_2$, (c) WS$_2$ selected at 500 rpm and (f) MoS$_2$ selected at 1.5 krpm devices. Relative change of resistance as a function of compressive strain for (d) WS$_2$, and (e) WS$_2$ selected at 1.5 krpm devices.

crystals, which is effectively transferred to them by the substrate [23]. Both behaviors are observed in our devices. As illustrated in figure 2(b), the change of resistivity increases while the tensile strain is being applied to the device made with the unselected dispersion of tungsten disulfide. This is because nanosheets move away from each other, thus increasing junction resistance. On the contrary, previous reports for TMDs mixed with PEO have shown that the strain applied to the composite is affected by the gauge factor (G_{NS}) of the TMDs, which is negative. This means that for every change in strain, there is a decrease in resistivity as shown in figure 2(c) for the device produced with the dispersion selected at 500 rpm.

The percolation theory have been used to explain the effect in composites with conductive fillers. In this case, the fillers form chains in which piezoresistivity and resistivity depend on the conductive filler and the junction between fillers [12, 23]. Not only the fillers

can be conductive, but also semiconductors, as studied by Biccai and coworkers with PEO based composites filled with TMDs. The resistivity of these composites is described by,

$$\rho = \frac{(R_{NS} + R_J)\,\chi}{l_{NS}} \qquad (2)$$

which is dependent on the resistance of the nanosheet R_{NS}, the resistance of the junctions R_J, the form of the structure χ, and the length of the nanosheets l_{NS}. In this model, the change of resistance is then given by 3,

$$\frac{dR}{R} = \left(\frac{G_{NS} + (dR_J/d\varepsilon)/R_{NS,0}}{1 + R_{J,0}/R_{NS,0}} + 2 \right)\varepsilon \qquad (3)$$

where $R_{NS,0}$ and $R_{J,0}$ are the nanosheet (NS) and junction resistance at zero-strain applied. Equation (3) describes that the change of resistance is due to a change in the nanosheet, a change in the junctions, and a change in the geometry of the composite.

The gauge factor is measured for both devices, as shown in figures 2(b) and (c), by fitting a linear model to the curve. As could be seen in figure 2(b) this is done for different strain percentages, as these devices change their GF as strain is applied, which has also been observed in other TMD-based sensors [10]. This same procedure is done for devices made with dispersions of centrifuge speeds of 1 and 1.5 krpm. Furthermore, the transport properties of the same devices were studied as a function of strain when a compressive strain was applied. The relative change of resistivity was extracted from these measurements and plotted as seen in figures 2(d), (e) and S2(b)–(e) for the devices made with the unselected and the size-selected dispersions of tungsten disulfide. As was also observed by Biccai and coworkers, in figure 2(e) a transition from a positive to a negative value of the gauge factor is observed.

From this point forward, we will concentrate on the gauge factor of the devices within the region close to 0.4%, which will serve as a standard for comparing both materials and their dependence on lateral size. Within this range all of the transport properties exhibit linearity and low hysteresis as strain is released as shown in figures S3 and S4 of the supplemental material. The gauge factor of unselected WS_2 is positive when tensile strain is applied (refer to figure 2(b)), and negative when compressive strain is applied, as shown in figure 2(d) and in the work of [26]. This could be explained by considering that as compressive strain is employed, the out-of-plane direction is also being strained and the piezoresistive matrix of the WS_2 printed on the PVDF filter exhibits anisotropic properties.

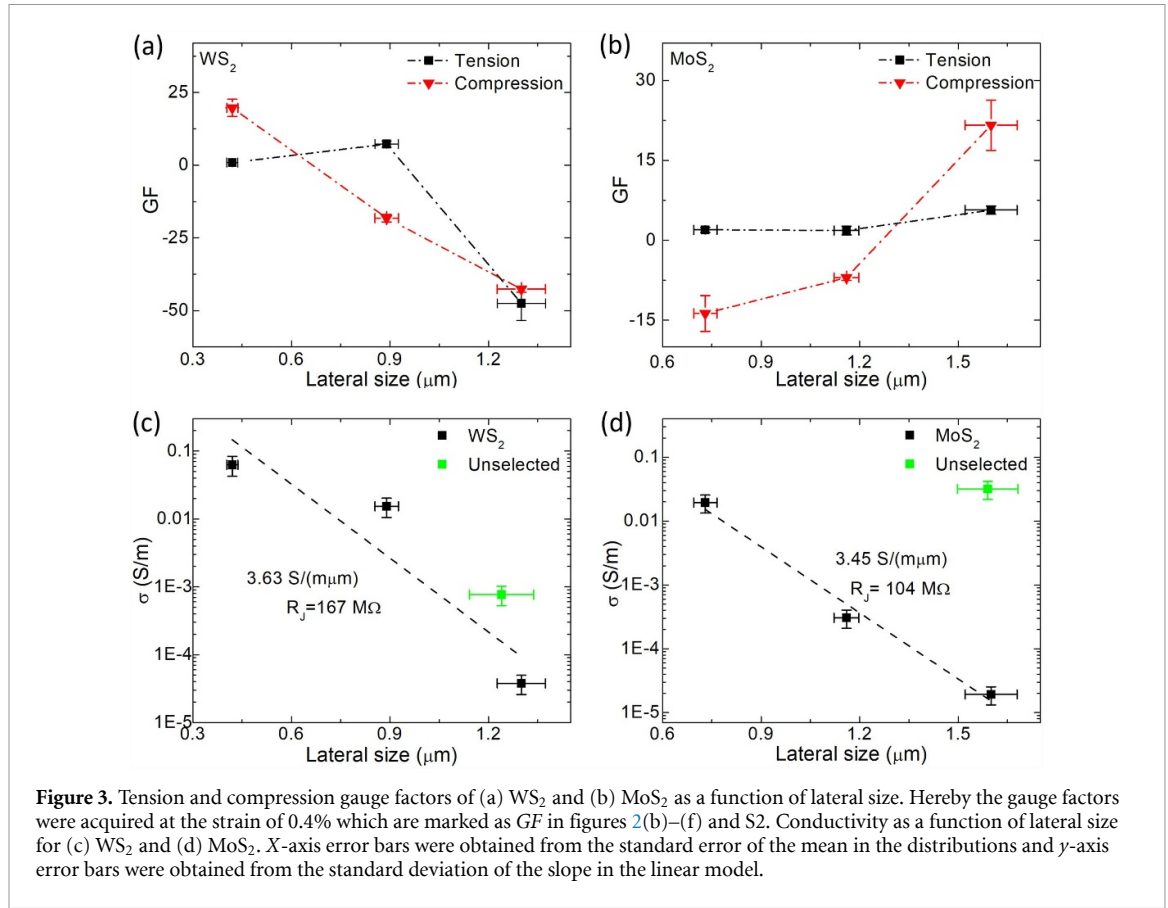The positive tensile GF is smaller than similar paper-based WS_2 devices [22], but the negative compressive GF is similar to the characterization done by Biccai and coworkers in composites of TMDs with PEO [23]. As the standardize strain limit is exceeded, unselected WS_2 networks exhibit a positive gauge factor (refer to figure 2(d)). It is possible that further exceeding the strain beyond 1.5% might result in another change in the *GF*, but additional experimentation would be required to test this.

Figure 3(a) shows the *GF* of WS_2 as a function of average lateral size. Its value reduces as lateral size increases, and there is a change from positive to negative when the lateral size is close to 1.0 μm for tensile strain and close to 0.6 μm for compressive strain, which is the first report of this transition mediated by lateral size of the nanosheets. These two results can be modeled through equation (3), where the change in resistivity depends on the intrinsic gauge factor of the nanosheets, which has been reported to be negative [17, 18], and the change of the junction resistance due to strain, which would be positive as the tensile strain causes tunneling barriers to increase, thus increasing the resistance [19]. In small-size WS_2 networks, $(dR_J/d\varepsilon)/R_{NS,0} > G_{NS}$, while in large-size networks, $(dR_J/d\varepsilon)/R_{NS,0} < G_{NS}$.

The *GF* for devices of WS_2 with smaller average lateral size of the nanosheets, is sensitive to the change of junction resistance due to strain. Conversely, the *GF* of WS_2 devices where the network is formed by larger nanosheets, is sensitive to their intrinsic gauge factor. Finally, it is observed in figure 3(a) that the absolute value of the tensile *GF* is bigger than the compressive *GF* for the large average lateral size devices, which is consistent with WS_2 devices printed on paper [22].

Furthermore, figures 2(f) and S2(f)–S2(l) of the supplemental material exhibit the change of resistivity as tensile and compressive strain is applied to unselected and size-selected molybdenum disulfide (MoS_2) devices. The value of the *GF* extracted from the unselected devices is of the same order for similar devices [23]. The device selected at a speed of 1.5 krpm shows a higher *GF* for a strain percentage lower than 0.07% compared to a lower *GF* for the standardized comparison strain (refer to figure 2(f)).

Figure 3(b) illustrates the response of the gauge factor as a function of lateral size for MoS_2. The *GF* exhibits different trends between tensile and compressive strains. Specifically, for tensile strain, the *GF* increases with lateral size and is always positive. On the contrary, for compressive strain, the *GF* increases with lateral size and the change of *GF* is from negative to positive, which is a first report of tuning the *GF* of MoS_2 with lateral size of nanosheets. Taking a look at the model detailed in equation (3), for the tensile test, in MoS_2 networks $(dR_J/d\varepsilon)/R_{NS,0} > G_{NS}$, while for the compression test, in small-size networks $(dR_J/d\varepsilon)/R_{NS,0} < G_{NS}$ and in large-size networks $(dR_J/d\varepsilon)/R_{NS,0} > G_{NS}$.

Figure 3. Tension and compression gauge factors of (a) WS_2 and (b) MoS_2 as a function of lateral size. Hereby the gauge factors were acquired at the strain of 0.4% which are marked as *GF* in figures 2(b)–(f) and S2. Conductivity as a function of lateral size for (c) WS_2 and (d) MoS_2. *X*-axis error bars were obtained from the standard error of the mean in the distributions and *y*-axis error bars were obtained from the standard deviation of the slope in the linear model.

This behaviour is opposed to what is observed for WS_2 and to understand why it differs, the conductivity of both TMDs was plotted as a function of lateral size as shown in figures 3(c) and (d). Their conductivity decreases with lateral size and it fits well to the linear model described by Coleman and coworkers for networks formed by arrays of semiconductive nanosheets with high junction resistance (R_J) in which conductivity depends on the nanosheet resistance and the junction resistance [32, 37]. In this model, the conductivity is described by (4)

$$\sigma_{Net} \approx \frac{l_{NS}k\phi^{\beta}}{R_j^2 e\mu_{NS}} \tag{4}$$

which is a function of the nanosheet volume fraction ϕ, a percolation exponent β, the aspect ratio k, and the nanosheet carrier mobility μ_{NS}.

The model allows to extract the junction resistance of both type of TMDs networks. As measured by Kelly and coworkers, in molybdenum diselenide ($MoSe_2$) networks the nanosheet mobility is approximately 91 cm^2 (Vs)$^{-1}$ and the volume fraction is almost 0.4 [38], also $\beta = 2.5$, as measured in WS_2 and graphene devices [39]. To calculate the junction resistance, those values are used, with the aspect ratio of WS_2, with a value of 1441 and MoS_2, with a value of

544, as determined in our work on photoconductive properties in similar devices [29].

WS_2 exhibits a larger junction resistance as compared to MoS_2. Furthermore, figure 3(c) shows that conductivity of tungsten disulfide is larger than that of molybdenum disulfide networks, which could be due to the reduced number of layers of WS_2, as they approach the monolayer and the bandgap increases when doing so [31]. Thus, as the compressive strain is applied to the large-size nanosheet network, the alignment of the NSs is arranged and as they move close to each other the resistivity drops because the junction resistance decreases. However, for the small-size nanosheet network, a negative *GF* indicates that as the nanosheet is being compressed, there is an increase in resistivity.

Both the difference in the type of transition from negative to positive when the size increases in contrast to what occurs in WS_2 and the deviation to the linear model in figure 3(c) could also be related to the difference in number of layers or to the difference in the c-axis lattice constant of the crystal structure in both of the TMDs, as XRD measurements have shown that WS_2 crystallizes in a 2 H structure, while MoS_2 crystallizes in a mixture of 3 R and 2 H structures (Refer to our work in the photoconductive properties tuned by the dimensions of TMDs in similar devices [29]).

Further research on the dependence of both features is out of the scope of this research.

4. Conclusions

The piezoresistivity was effectively measured in liquid-phase exfoliated, mediated by intercalation, TMDs networks printed on PVDF membrane filter. For tungsten disulfide (WS_2) devices, the gauge factor varies from 25 to -50 and both at a tensile and compressive uniaxial strain there is a transition from positive to negative *GF* as average size increases. Molybdenum disulfide networks exhibit *GF* from 1 to 7 as a tensile uni-axial strain is applied and -15 to 22 as a compressive strain is applied. Only at a compressive strain, the *GF* transitions from a negative to a positive value as nanosheet size increases. As described, the gauge factor depends on the intrinsic *GF* of the nanosheet and on the change of junction resistance due to strain.

Furthermore, the conductivity of these networks increases as nanosheet length decreases. These are modeled as networks of pairs of nanosheets and junction, each having their own resistance. Tungsten disulfide networks have a higher network conductivity as opposed to molybdenum disulfide, yet they exhibit a higher junction resistance. Moreover, at a tensile strain, when the nanosheet size of WS_2 is large, the gauge factor of the nanosheet dominates the *GF* of the network. Finally, at a compressive strain, in both large-size WS_2 and small-size MoS_2 networks, the gauge factor of the NS dominates that of the network.

Data availability statement

All data that support the findings of this study are included within the article (and any supplementary material).

Acknowledgments

ORCID iDs

D Olaya-Cortes ● https://orcid.org/0009-0006-6758-1649
T Rubio ● https://orcid.org/0009-0005-1006-4758
P Giraldo-Gallo ● https://orcid.org/0000-0002-2482-7112
Y Hernandez ● https://orcid.org/0000-0002-6980-8820

References

[1] Desai S B, Seol G, Seuk Kang J, Fang H, Battaglia C, Kapadia R, Ager J W, Guo J and Javey A 2014 Strain-induced indirect to direct bandgap transition in multilayer WSe_2 *Nano Lett.* **14** 4592–7

[2] Wang Y, Cong C, Yang W, Shang J, Peimyoo N, Chen Y, Kang J, Wang J, Huang W and Ting Y 2015 Strain-induced direct–indirect bandgap transition and phonon modulation in monolayer WS_2 *Nano Res.* **8** 2562–72

[3] Ghorbani-Asl M, Borini S, Kuc A and Heine T 2013 Strain-dependent modulation of conductivity in single-layer transition-metal dichalcogenides *Phys. Rev.* B **87** 235434

[4] Rice C, Young R J, Zan R, Bangert U, Wolverson D, Georgiou T, Jalil R and Novoselov K S 2013 Raman-scattering measurements and first-principles calculations of strain-induced phonon shifts in monolayer MoS_2 *Phys. Rev.* B **87** 081307

[5] Feng J, Qian X, Huang C-W and Li J 2012 Strain-engineered artificial atom as a broad-spectrum solar energy funnel *Nat. Photon.* **6** 866–72

[6] Conley H J, Wang B, Ziegler J I, Haglund R F J, Pantelides S T and Kirill I B 2013 Bandgap Engineering of Strained Monolayer and Bilayer MoS_2 *Nano Lett.* **13** 3626–30

[7] He K, Poole C, Fai Mak K and Shan J 2013 Experimental demonstration of continuous electronic structure tuning via strain in atomically thin MoS_2 *Nano Lett.* **13** 2931–6

[8] Zhu C R *et al* 2013 Strain tuning of optical emission energy and polarization in monolayer and bilayer MoS_2 *Phys. Rev.* B **88** 121301

[9] Feierabend M 2019 Dark exciton based strain sensing in tungsten-based transition metal dichalcogenides *Phys. Rev.* B **99** 195454

[10] Shi F, Juanrui D, Han Q, Zhang F, Wang K, Kan Z, Wang L, Chunyan Li and Lin X 2023 Integrated wearable foam modified with WS_2 nanosheets@MoS_2 quantum dots for oral disease diagnosis and healthcare monitoring *Chem. Eng. J.* **477** 146800

[11] Roldán R, Castellanos-Gomez A, Cappelluti E and Guinea F 2015 Strain engineering in semiconducting two-dimensional crystals *J. Phys.: Condens. Matter* **27** 313201

[12] Chung D D L 2020 A critical review of piezoresistivity and its application in electrical-resistance-based strain sensing *J. Mater. Sci.* **55** 15367–96

[13] Junli D, Huihui Y, Liu B, Hong M, Liao Q, Zhang Z and Zhang Y 2021 Strain engineering in 2D material-based flexible optoelectronics *Small Methods* **5** 2000919

[14] Carrascoso F, Hao Li, Frisenda R and Castellanos-Gomez A 2021 Strain engineering in single-, bi- and tri-layer MoS_2, $MoSe_2$, WS_2 and WSe_2 *Nano Res.* **14** 1698–703

[15] Feng Li, Shen T, Wang C, Zhang Y, Junjie Q and Zhang H 2020 Recent advances in strain-induced piezoelectric and piezoresistive effect-engineered 2D semiconductors for adaptive electronics and optoelectronics *Nano-Micro Lett.* **12** 106

[16] Blundo E, Cappelluti E, Felici M, Pettinari G and Polimeni A 2021 Strain-tuning of the electronic, optical and vibrational properties of two-dimensional crystals *Appl. Phys. Rev.* **8** 021318

[17] Tsai M-Y, Tarasov A, Hesabi Z R, Taghinejad H, Campbell P M, Joiner C A, Adibi A and Vogel E M 2015 Flexible MoS_2 field-effect transistors for gate-tunable piezoresistive strain sensors *ACS Appl. Mate. Int.* **7** 12850–5

[18] Manzeli S, Allain A, Ghadimi A and Kis A 2015 Piezoresistivity and strain-induced band gap tuning in atomically thin MoS_2 *Nano Lett.* **15** 5330–5

[19] Yokaribas V, Wagner S, Schneider D S, Friebertshäuser P, Lemme M C and Fritzen C-P 2017 Strain gauges based on CVD graphene layers and exfoliated graphene nanoplatelets with enhanced reproducibility and scalability for large quantities *Sensors* **17** 2937

[20] Wagner S *et al* 2018 Highly sensitive electromechanical piezoresistive pressure sensors based on large-area layered PtSe$_2$ films *Nano Lett.* **18** 3738–45

[21] Zhang R *et al* 2024 High-performance piezoresistive sensors based on transfer-free large-area **PdSe$_2$** films for human motion and health care monitoring *InfoMat* **6** e12484

[22] Zhang W, Frisenda R, Zhao Q, Carrascoso F, Al-Enizi A M, Nafady A and Castellanos-Gomez A 2021 Paper-supported WS$_2$ strain gauges *Sens. Actuators* A **332** 113204

[23] Biccai S, Boland C S, O'Driscoll D P, Harvey A, Gabbett C, O'Suilleabhain D R, Griffin A J, Zheling Li, Young R J and Coleman J N 2019 Negative gauge factor piezoresistive composites based on polymers filled with MoS$_2$ nanosheets *ACS Nano* **13** 6845–55

[24] Riyajuddin S, Kumar S, Gaur S P, Sud A, Maruyama T, Ehesan Ali Md and Ghosh K 2020 Linear piezoresistive strain sensor based on graphene/g-C$_3$N$_4$/PDMS heterostructure *Nanotechnology* **31** 295501

[25] Selamneni V, Koduvayur Ganeshan S, Nerurkar N, Akshaya T and Sahatiya P 2021 Facile fabrication of MoSe$_2$ on paper as an electromechanical piezoresistive pressure–strain sensor *IEEE Transac. Instrumen. and Meas.* **70** 6002408

[26] Varghese A, Pandey A H, Sharma P, Yin Y, Medhekar N V and Lodha S 2024 Electrically controlled high sensitivity strain modulation in MoS$_2$ field-effect transistors via a piezoelectric thin film on silicon substrates *Nano Lett.* **24** 8472–80

[27] Olaya-Cortes D E 2024 Lateral size dependence of piezoresistivity and photoconductivity in TMD networks *PhD Thesis* Universidad de los Andes: (https://doi.org/10.57784/1992/74906)

[28] Coleman J N *et al* 2011 Two-dimensional nanosheets produced by liquid exfoliation of layered materials *Science* **331** 568–71

[29] Olaya-Cortes D, Ramos-Moreno L, Rubio Cruz T, Pabón Londoño J P and Hernandez Y 2024 Lateral size dependence of photoconductivity in TMD networks *J. Phys.: Condens. Matter.* **37** 075301

[30] Ueberricke L, Coleman J N and Backes C 2017 Robustness of size selection and spectroscopic size, thickness and monolayer metrics of liquid-exfoliated WS$_2$ *Phys. Status Solidi* b **254** 1700443

[31] Backes C *et al* 2016 Production of highly monolayer enriched dispersions of liquid-exfoliated nanosheets by liquid cascade centrifugation *ACS Nano* **10** 1589–601

[32] Kelly A G, O'Suilleabhain D, Gabbett C and Coleman J N 2022 The electrical conductivity of solution-processed nanosheet networks *Nat. Rev. Mater.* **7** 217–34

[33] Costa Moura C, Tare R S, Oreffo R O C and Mahajan S 2016 Raman spectroscopy and coherent anti-stokes raman scattering imaging: prospective tools for monitoring skeletal cells and skeletal regeneration *J. R. Soc. Interface* **13** 20160182

[34] Berkdemir A *et al* 2013 Identification of individual and few layers of WS$_2$ using Raman Spectroscopy *Sci. Rep.* **3** 1755

[35] Song-Lin Li, Miyazaki H, Song H, Kuramochi H, Nakaharai S and Tsukagoshi K 2012 Quantitative Raman spectrum and reliable thickness identification for atomic layers on insulating substrates *ACS Nano* **6** 7381–8

[36] Fiorillo A S, Critello C D and Pullano S A 2018 Theory, technology and applications of piezoresistive sensors: a review *Sens. Actuators* A **281** 156–75

[37] Gabbett C *et al* 2023 Quantifying the contribution of material and junction resistances in nano-networks (arXiv:2311.16740 [cond-mat])

[38] Kelly A G 2017 All-printed thin-film transistors from networks of liquid-exfoliated nanosheets *Science* **356** 69–73

[39] O'Suilleabhain D, Vega-Mayoral V, Kelly A G, Harvey A and Coleman J N 2019 Percolation effects in electrolytically gated WS$_2$/Graphene nano:nano composites *ACS Appl. Mater. Int.* **11** 8545–55